ELSEVIER

Cement & Concrete Composites 24 (2002) 7–15

Cement & Concrete Composites

www.elsevier.com/locate/cemconcomp

Use of EIS, ring-disk electrode, EQCM and Raman spectroscopy to study the film of oxides formed on iron in 1 M NaOH

S. Joiret [a], M. Keddam [a], X.R. Nóvoa [b,*], M.C. Pérez [b], C. Rangel [c], H. Takenouti [a]

[a] UPR 15 du CNRS, C. P. 133, 4 Place Jussieu, 75252 Paris Cedex 05, France
[b] University of Vigo, E.T.S.E.I.M, Lagoas-Marcosende 9, 36280 Vigo, Spain
[c] INETI, Estrada do Paço do Lumiar, 1699 Lisboa Codex, Portugal

Abstract

Different electrochemical techniques (electrochemical impedance spectroscopy (EIS), ring-disk electrode, electrochemical quartz crystal microbalance (EQCM), and in situ Raman spectroscopy) have been employed to study the behaviour of the passive film formed on iron in alkaline medium simulating pore solution in fresh concrete. The study, based on low scan rate cyclic voltammetry performed over the entire electrolyte stability domain, allows for establishing the influence of the redox activity developing in the oxides layer on the electrochemical behaviour of the system and, thus, to get valuable information on the applicability of classical electrochemical techniques employed to assess corrosion of steel in concrete.

The passive film is based on a magnetite-type structure which, in partially reversible processes, can be oxidised and reduced depending on the electrode potential. Those redox processes mask the corrosion process itself. © 2002 Elsevier Science Ltd. All rights reserved.

Keywords: EIS; EQCM; Raman spectroscopy; Oxides

1. Introduction

Since the late 1980s the corrosion rate of steel rebar in concrete is commonly measured by polarisation resistance method [1,2], *Rp*, based upon the Stern–Geary equation $i_{corr} = B/Rp$ [3]. Moreover, all over the 1990s different electrochemical methods have also been used for this purpose [4]. Potentiostatic and galvanostatic pulses [5,6], electrochemical impedance spectroscopy (EIS) [7] and cyclic voltammetry [8,9], can be cited among the techniques devoted to get the *Rp* parameter. Although numerous authors have carried out studies relative to the iron in alkaline medium [10–16], the dissolution and passivation mechanisms remain still unclear and only recently [17] an interpretation has been advanced on the physical basis for measuring *Rp* not at the steady-state, but to a certain sweep rate/waiting time, as empirically stated in [1].

The present paper is aimed to investigate the different redox processes taking place on the iron electrode in a strongly alkaline medium in order to better understand the passivity and passivity breakdown of steel rebars in concrete. This will also help in *Rp* interpretation over the full range of possible rebar corrosion potentials. Different electrochemical techniques, cyclic voltammetry, EIS, quartz microbalance, in situ Raman spectroscopy, and ring-disk electrode were used for this sake.

2. Experimental conditions

Electrolyte. 1 M NaOH solutions were prepared with a reagent grade chemical (Prolabo) and doubly deionised water. This solution was chosen because the redox processes in the passive layer are well differentiated and it is not far from the alkalinity found in cement pastes prepared from standard Portland cement. For a cement paste prepared with water to cement ratio equal to 0.5, at 180 days ageing, the ionic concentrations in pore water are $[OH^-] = 0.32$ to 0.71 M, $[Na^+] = 0.08$ to 0.16 M and $[K^+] = 0.24$ to 0.55 M, the upper limit corresponding to highly alkaline cements [18]. All experiments were carried out without electrolyte agitation, except in the ring-disk experiments where

* Corresponding author. Tel.: +34-986-812-213; fax: +34-986-812-201.
E-mail address: rnovoa@uvigo.es (X.R. Nóvoa).

0958-9465/02/$ - see front matter © 2002 Elsevier Science Ltd. All rights reserved.
PII: S0958-9465(01)00022-1

the working electrodes were introduced in an impinging jet cell. The Reynolds number of the electrolyte flow was 350.

Electrochemical cell. All measurements were carried out using the classical three-electrode arrangement. The reference electrodes employed were Hg/HgO/KOH 1 M and saturated calomel electrode (SCE). In this paper all potentials are referred to the SCE because this electrode is the most employed for measurements on concrete rebars in the laboratory. The counter-electrode was a platinum gauze of large surface. Finally, an iron rod ($\varnothing = 5$ mm) from Goodfellow was used as working electrode for all experiments except quartz crystal microbalance measurements. The iron rod was covered with a cataphoretic paint and embedded in epoxy resin. The external diameter was worked to 18 mm. Before each experiment the electrode surface was polished with emery paper up to #1200 grade, degreased and washed with water. In the ring-disk experiments, the iron rod was covered on its lateral part only by cataphoretic paint, which also isolates electrically the ring and disk electrodes. The ring was the cross-section of a vitreous carbon tube of 5.1 mm internal diameter and 7 mm external diameter. The theoretical collection efficiency, N_0 was 0.463. For the electrochemical quartz crystal microbalance (EQCM) experiments, the iron was electrodeposited on a gold electrode. A heat treatment allowed absorbed hydrogen elimination.

Electrochemical instrumentation and setup. Voltammograms were obtained by using the potentiostat PGSTAT20 (from Ecochimie) at 0.5 mV s^{-1} on stationary electrode. Solartron equipment (ECI 1286 + FRA 1255) was used for impedance measurements. This equipment was coupled with an analogue filter (Kemo, VBF 8), to improve the signal to noise ratio. The impedance system was controlled via IEEE by a personal computer using the FraCom 2.1 program devised by UPR 15. The electrode impedance was measured between 1 kHz and 1 mHz in frequency decreasing sweep (five points per decade) with ac potential perturbation of 10 mV (rms) amplitude.

For the ring-disk measurements (impinging jet cell), a home made bi-potentiostat was employed to control ring and disk potentials. A triangular signal generator (Eurelco, Model D311) allowed sweeping the disk potential at 1 mV s^{-1} and a multi-channel voltmeter (Keithley 199) under remote control collected disk and ring potentials and currents.

In situ Raman spectra were recorded during electrochemical experiments by using a green Ar laser beam (514.5 nm) for excitation at 10 mW intensity, a microscope with long focal objective (Olympus, UL WD MS PL 80X/0.75) and a Dilor spectrophotometer. The air-cooled CCD detector allowed spectra to be taken within 300 s of exposure to the laser light. Data acquisition, storage and treatment were carried out with a personal computer, using Dilor's specific software.

The equipment for EQCM measurements was: an oscillator for 9 MHz AT quartz, manufactured in the UPR15, a frequency counter (Schlumberger, universal counter 2721), a potentiostat–galvanostat (Sotelem, PG-stat-Z1), a signal generator (Eurelco, D311) and a multi-channel voltmeter (Keithley 199). The FRQM program (devised by UPR 15) monitored electrode potential, current and quartz oscillation frequency. Voltammograms and voltamassograms (m(E)) were obtained at 1 mV s^{-1} potential sweep rate.

3. Results

3.1. Cyclic voltammetry

Fig. 1 shows the first cycle voltammogram obtained on a stationary iron electrode at sweep rate $dE/dt = 0.5$ mV s^{-1}. Six oxidation peaks are observed in the forward (anodic) sweep and five reduction peaks in the reverse (cathodic) sweep. The peaks are numbered in the figure I–VI and VII–XI, respectively. The peaks III, V, VI, VII and X are not reported in the reviewed literature. These peaks have only been observed with the stationary electrode and at very low potential sweep rate [19].

3.2. In situ Raman spectroscopy

The Raman spectra were obtained at selected potential values between −1.5 and 0.5 V by sweeping hold at the desired potential in both forward and reverse scans. As in the first cycle the obtained Raman signals were not

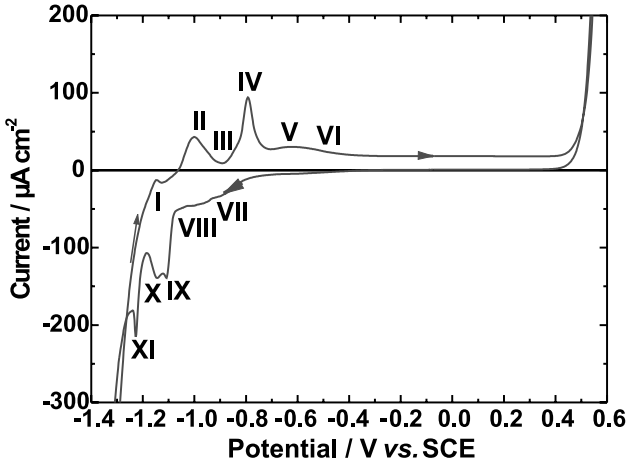

Fig. 1. First cycle of the voltammogram obtained for the stationary Fe electrode in 1 M NaOH at $dE/dt = 0.5$ mV s^{-1}. Current peaks are consecutively noted by I–XI.

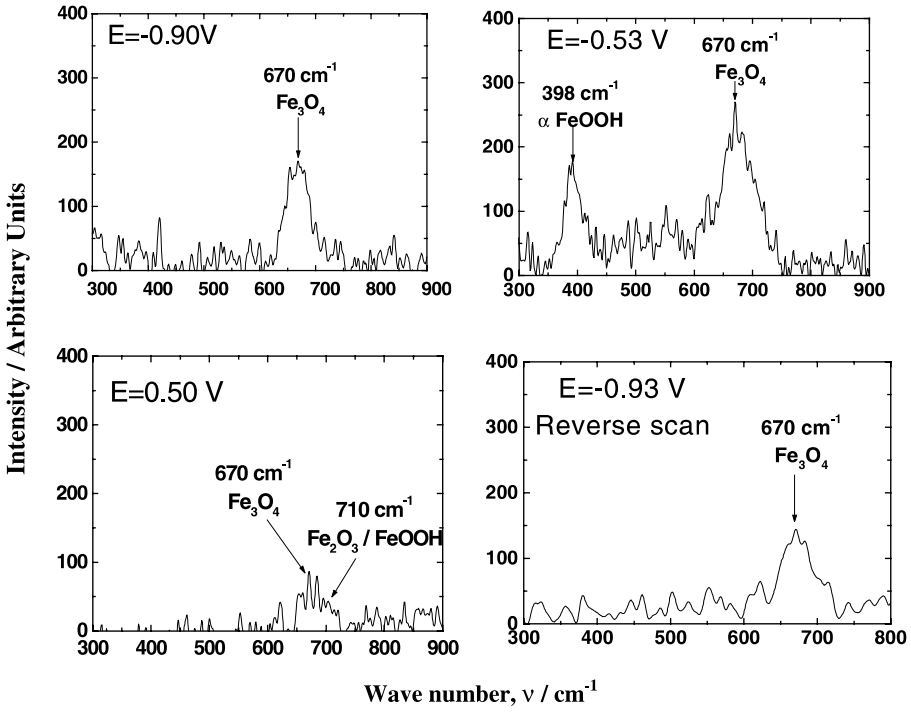

Fig. 2. In situ Raman spectra of the stationary Fe electrode in 1 M NaOH at the different polarisation potentials in the forward (anodic) (Fig. 2(a)–(c)) and reverse (cathodic) scan (Fig. 2(d)).

sufficiently well resolved, it was necessary to cycle the electrode potential for 2 h at 10 mV s^{-1}. Fig. 2 depicts some spectra obtained at potentials corresponding to the forward scan (Fig. 2(a)–(c)) and to the reverse scan (Fig. 2(d)).

Fig. 2 shows the presence of magnetite (Fe_3O_4), characterised by the peak at 670 cm^{-1} in all the examined potential range, even at −0.9 V (Fig. 2(a) and (d)) in both anodic and cathodic scans. In Fig. 2(b), at the potential of peak VI (−0.53 V), the presence of α-FeOOH is also observed (peak at 398 cm^{-1}). For potential values more anodic than the corresponding to peak VI (Fig. 2(c)), the magnetite signal decreases and a new peak appears at 710 cm^{-1}. This wave number corresponds to γ-Fe_2O_3 (magemite) and/or its hydrated form γ-FeOOH that will result from partial oxidation of magnetite.

3.3. Electrochemical impedance spectroscopy

EIS measurements were carried out on the stationary iron electrode in the whole potential interval examined in the cyclic voltammetry. Figs. 3 and 4 illustrate two of the spectra obtained. The presence of two time constants was observed for all spectra. The results of the EIS measurements have been successfully fitted to a hierarchically distributed equivalent circuit (Fig. 3) using a simplex method already described [20]. The impedance of this circuit, $Z(\omega)$, at the angular frequency ω is given in Eq. (1). The α_1 and α_2 parameters model the Cole–Cole type dispersion of the time constants R_1C_1 and R_2C_2 that reproduce the depressed semicircles found in the impedance's complex plane plots.

$$Z(\omega) = R_0 + \frac{R_1}{\frac{1}{1+(Z_2(\omega)/R_1)} + (j\omega R_1 C_1)^{\alpha_1}} \quad \text{being } Z_2(\omega) = \frac{R_2}{1 + (j\omega R_2 C_2)^{\alpha_2}}. \tag{1}$$

The impedance results are compatible with the different oxidation–reduction reactions corresponding to a blocking electrode process with a small dc current leakage.

Fig. 5 shows the potential dependence of capacitances C_1 and C_2, corresponding respectively to the time constants observed in higher and in lower frequency range.

In Fig. 5, it can be seen that C_1 varies between 0.05 and 1 mF cm^{-2}. Since this capacitance corresponds to the time constant observed in the high frequency range, it may be assigned to the double layer capacitance. Nevertheless the obtained values are too high for this capacitance (specially for potential values lower than about −0.4 V). The real surface area with the roughness introduced by oxide layer might be considered to be very large. On the other hand, C_2 varies between 0.22 and 75 mF cm^{-2}. The values of C_2 are reasonable to be

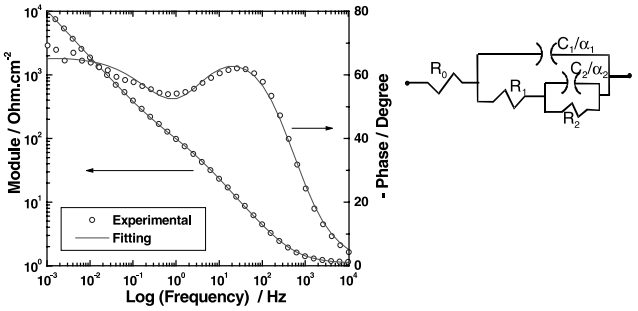

Fig. 3. Impedance spectrum (left) obtained for the stationary Fe electrode in 1 M NaOH at $E = -0.975$ V. Experimental results were fitted using two hierarchically distributed RC time constants (right) according to Eq. (1). The best-fitting parameters are: $R_0 = 1.1\ \Omega\ cm^2$, $R_1 = 150\ \Omega\ cm^2$, $C_1 = 1.08\ \mu F\ cm^{-2}$, $\alpha_1 = 0.7960$, $R_2 = 1.23\ M\Omega\ cm^2$, $C_2 = 69.3\ mF\ cm^{-2}$, $\alpha_2 = 0.7087$.

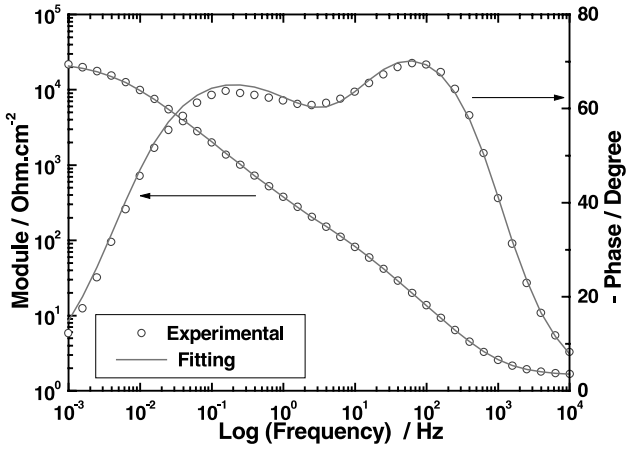

Fig. 4. Impedance spectrum obtained for the stationary Fe electrode in 1 M NaOH at $E = -0.45$ V. Experimental results were fitted using two hierarchically distributed RC time constants according to Eq. (1). The best-fitting parameters are: $R_0 = 1.6\ \Omega\ cm^2$, $R_1 = 236\ \Omega\ cm^2$, $C_1 = 179\ \mu F\ cm^{-2}$, $\alpha_1 = 0.8779$, $R_2 = 23.4\ k\Omega\ cm^2$, $C_2 = 1.03\ mF\ cm^{-2}$, $\alpha_2 = 0.7425$.

attributed to the different redox processes taking place on the electrode.

3.4. Ring-disk electrode results

Fig. 6 depicts some of the results obtained by the ring-disk experiments at 1 mV s^{-1} disk potential sweep rate. The first three cycles are presented. The experiments were performed with two different ring potential values, one to collect Fe^{2+} leaving the disk (ring potential $E_{ring} = +0.125$ V) and another to detect Fe^{3+} emitted form the disk ($E_{ring} = -1.13$ V).

It was found that the emission of Fe^{2+} from the disk decreases monotonically as the disk potential increases. When the disk potential was swept to more anodic potential (−1.5 to −1.3 V), the ring current decreases as the

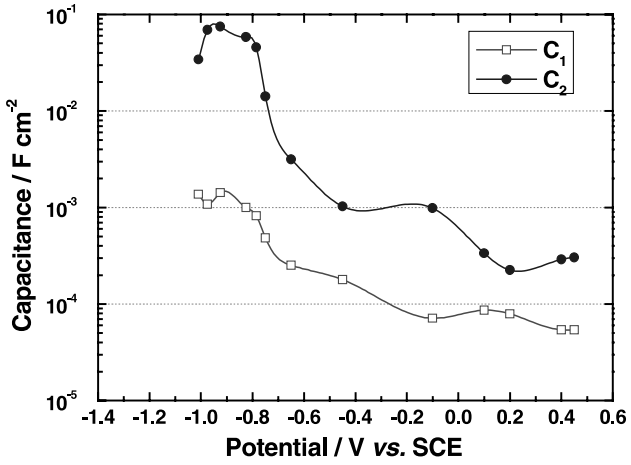

Fig. 5. Electrode potential dependence of capacitances C_1 and C_2. These values were obtained by fitting experimental impedance data (from the stationary Fe electrode in 1 M NaOH) to Eq. (1).

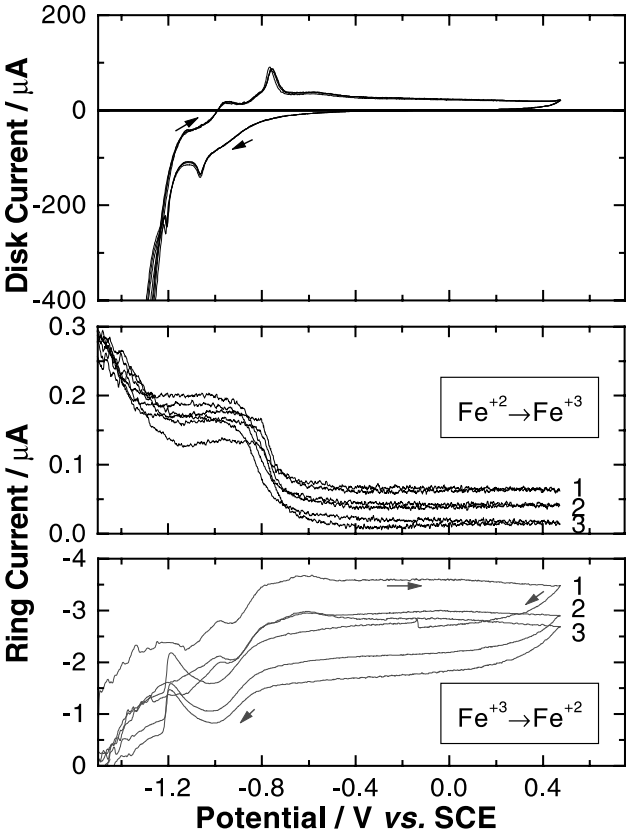

Fig. 6. RDE experiments. Iron disk ($\varnothing = 5$ mm) and glassy carbon ring ($\varnothing_{in.} = 5.1$ mm, $\varnothing_{ext.} = 7$ mm). Collection efficiency $N_0 = 0.463$. $dE_{disk}/dt = 1$ mV s^{-1}. The labels in the figure correspond respectively to the 1st, 2nd and 3rd cycles of disk potential sweep. The ring potential for collection of Fe^{3+} was −1.13 V, and that for Fe^{2+} was +0.125 V vs SCE.

cathodic current at the disk diminishes. The ring current in this potential range is therefore likely related to the oxidation of hydrogen formed at the disk. Later on, in

the potential range between peaks I and III ($-1.2 < E < -0.8$ V), the ring current remains constant, and valued about 0.2 μA. Only a small part of the disk current is therefore used to the formation of soluble Fe^{2+} species. For the potential above the peak IV ($E > -0.7$ V), the amount of Fe^{2+} detected was tiny at the ring, and the emission of this species vanishes at each potential cycle.

At the same time, Fe^{3+} detected at the ring increases in general with disk potential with badly defined peaks up to −0.5 V. The position of those peaks corresponds respectively to peaks II, III and V observed in Fig. 1 (the anodic sweep of cyclic voltammogram). For the potential sweep of the disk towards more cathodic potentials, the Fe^{3+} ring current remains almost constant down to −0.7 V, and then it decreases down to −1 V, that is, in the potential domain corresponding to peaks VII and VIII. Later on, an increase of Fe^{3+} emission can be seen down to −1.2 V corresponding to peaks IX–XI. A steep decrease can then be seen beyond peak XI.

3.5. Quartz crystal microbalance results

In Fig. 7, the results obtained by EQCM measurements are shown. The electrode potential has been cyclically swept (three cycles) between −1.5 and 0.5 V at 1 mV s^{-1}.

A significant mass loss from cycle to cycle can be remarked in Fig. 7. During the anodic sweep, the electrode mass decreases up to −1.1 V, potential close to the initiation of peak II (Fig. 1) and it increases slightly in the potential corresponding to peak III. This is an important result since the existence of peak III on voltammograms is often difficult to visualise. Afterwards

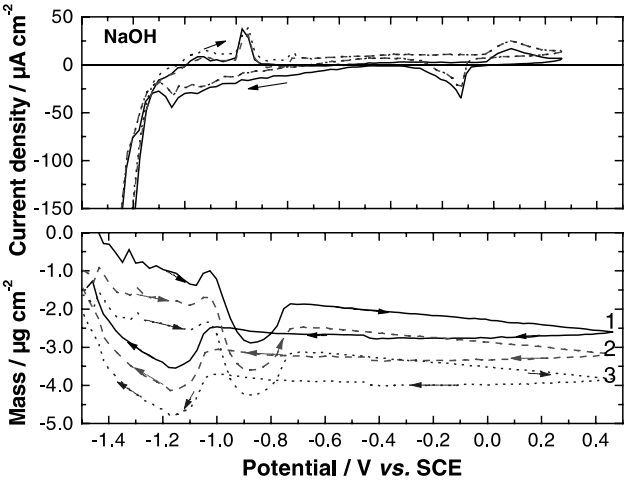

Fig. 7. Quartz crystal microbalance measurements on stationary electrode of electrodeposited Fe (∅ = 5 mm) in 1 M NaOH. Potential sweep rate = 1 mV s^{-1}. The labels in the figure correspond respectively to the 1st, 2nd and 3rd cycles of electrode potential sweep.

the mass decreases markedly in the potential domain of peak IV and then it increases in the potential range of peak V. A gradual mass loss takes place beyond peak V.

In the curve, during the cathodic potential sweep, the electrode mass remains essentially constant down to the potential corresponding to peak IX. In the potential domain of peaks IX and XI, the mass decreases. Beyond this potential, and when the hydrogen gas evolution is taking place at the electrode, the mass increases significantly. If anodic or cathodic sweeps are compared at each cycle, it can be seen that they are almost parallel each other, and the mass loss by cycle is evaluated to be about 0.6 μg cm^{-2}.

On the polarisation curve, it is also remarked a current peak at about 0.05 V during the anodic sweep and corresponding cathodic peak at about −0.15 V. This phenomenon is closely related to the nature of iron itself. It is important to note that similar peaks were also observed, in certain circumstances, on a mild steel specimen used as rebar material [21]. This redox process is not associated to a mass change. According to Pourbaix diagram for iron and the experiences on ferrate production in alkaline media [22], the transformation Fe^{3+}/Fe^{6+} can be considered the cause of the observed peaks.

4. Discussion

The different peaks observed in the voltammogram of Fig. 1 are assigned as follows.

The peak I, observed at very a cathodic potential (−1.2 V), is attributed to the reduction of the adsorbed hydrogen on the iron surface formed during the cathodic polarisation. Consequently, it is not directly related to the oxidation–reduction processes involving iron species.

The anodic peaks II and III and the cathodic peaks X and XI are assigned to the redox processes between Fe^0 and Fe^{+2} forming $Fe(OH)_2$ or FeO according to Eqs. (2) and (3).

$$Fe + 3H_2O \rightleftharpoons FeO + 2H_3O^+ + 2e^- \quad (2)$$

$$Fe + 4H_2O \rightleftharpoons Fe(OH)_2 + 2H_3O^+ + 2e^- \quad (3)$$

Though the origin of peak III is not clearly established, it is postulated that there are two Fe^0 species having different energy state. One possibility is that Fe^0 formed during the cathodic polarisation have two different energy states, for instance one near the oxide surface and another dispersed in the oxide interstices. Another possible source for this Fe^0 is the disproportionation reaction, according to Eq. (4), of the FeO or $Fe(OH)_2$ in the passive layer [23,24] formed by the process associated to peak II. At the potential corresponding to peak

III, the transformation of Fe^{II} may take place. The oxidation of Fe^0 thus formed gives rise to peak III.

$$4FeO \rightarrow Fe^0 + Fe_3O_4 \quad (4)$$

It is also possible that small interstitial particles of Fe^0 are formed in the surface film during the cathodic polarisation ($E < -1.25$ V) [25].

Peaks IV and IX are due to the formation of magnetite (Fe_3O_4) according to Eqs. (5) and (6):

$$3Fe(OH)_2 + 2OH^- \rightleftharpoons Fe_3O_4 + 4H_2O + 2e^- \quad (5)$$

$$3FeO + 2OH^- \rightleftharpoons Fe_3O_4 + H_2O + 2e^- \quad (6)$$

Peaks V and VI (anodic sweep) and VII and VIII (cathodic sweep) are attributed to the formation of two different Fe^{3+} species obtained from magnetite oxidation, according to the following reactions:

$$2Fe_3O_4 + 2OH^- \rightleftharpoons 3\gamma\text{-}Fe_2O_3 + H_2O + 2e^- \quad (7)$$

$$Fe_3O_4 + OH^- + H_2O \rightleftharpoons 3\alpha\text{-}FeOOH + e^- \quad (8)$$

The reaction (8) needs less energy because of topotactic nature of the reaction thus may correspond to the peaks V and VIII.

The electric charge, Q, involved for each peak observed in the voltammogram of Fig. 1 has been evaluated in order to verify its compatibility with the reactions above proposed. The evaluation has been performed according to Eq. (9)

$$Q = \int i\,dt = \int C\frac{dE}{dt}dt = \int C\,dE. \quad (9)$$

To analyse the curve $C(E)$ a Gaussian function has been considered for peak convolution. The obtained results are depicted in Figs. 8 and 9.

The calculated charge for each peak is summarised in Table 1.

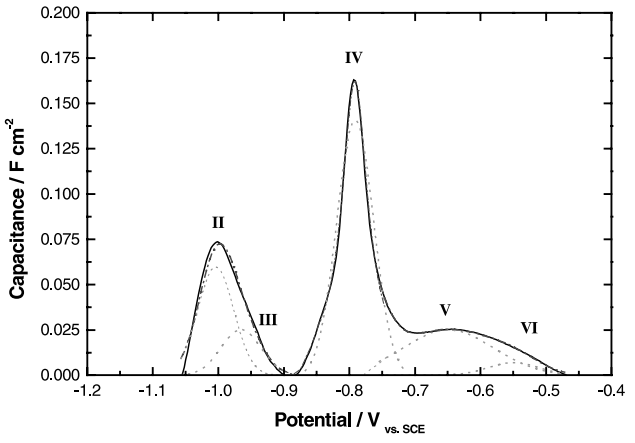

Fig. 8. Gaussian convolution of peaks found in the forward (anodic) branch of the voltammogram given in Fig. 1. Charge involved for each peak is given in Table 1.

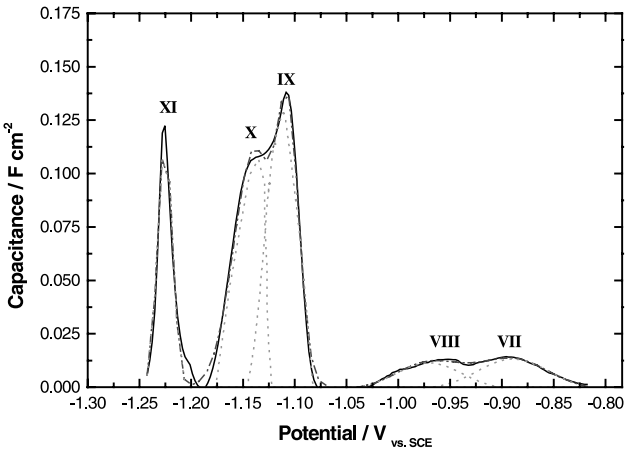

Fig. 9. Gaussian convolution of peaks found in the reverse (cathodic) branch of the voltammogram given in Fig. 1. Charge values are given in Table 1.

Table 1 shows that the charges associated to peaks III–VI are close to that determined for the corresponding cathodic peaks, VII–X. This observation corroborates therefore the association of different peaks made above. The charge involved in peak II is, on the contrary, twice that determined for peak XI. This discrepancy can be explained as follows. The reduction of Fe^{2+} at peak XI is not complete, but Fe^0 continues forming during the cathodic polarisation, in parallel to the hydrogen evolution reaction. The presence of magnetite at highly cathodic potential was verified experimentally by in situ Raman spectra (Fig. 2(a) and (d)). This Fe^0 species, as postulated above, is essentially located near the film surface. If Fe^0 involved in peak III is entirely formed by the reaction depicted by Eq. (4), the charge of peak III should be one fourth of that of peak II. Table 1 indicates that this ratio is practically one half. This remark corroborates the formation of interstitial Fe^0 during the cathodic polarisation. According to Eqs. (5) and (6), the charge associated to peak IV should be one third of the sum of peak II and III, whereas the observed value is much bigger. This fact coincides again with the presence of magnetite in very cathodic potential. As observed by ring-disk electrode experiments, Fe^{2+} and Fe^{3+} are leaving the disk in very cathodic potential (see Fig. 6). This may indicate that the magnetite transforms in this range to Fe^0, Fe^{2+}, and Fe^{3+}. A fraction of Fe^{2+} and Fe^{3+} thus formed will leave the electrode, and another will be trapped inside the surface film. The interstitial Fe^{2+} may contribute to the process observed by peak IV.

According to Eqs. (7) and (8), the sum of charge involved in peaks V and VI is one third of that needed to completely transform magnetite formed at peak IV into ferric oxide. Table 1 indicates that only one sixth of charge is found to forming the latter species. That is to

Table 1
Peak potential, E_{peak}, and charge, Q, obtained from convolution of peaks in Figs. 8 and 9

	Anodic sweep (Fig. 8)					Cathodic sweep (Fig. 9)				
Peak	II	III	IV	V	VI	VII	VIII	IX	X	XI
E_{peak}/V_{SCE}	−1.00	−0.96	−0.79	−0.65	−0.55	−0.88	−0.97	−1.12	−1.13	−1.23
Q/mC cm^{-2}	4.1	1.9	8.5	0.9	0.7	0.8	0.9	6.6	1.6	2.1

say, at each potential cycle (at least up to 3 cycles, maximum cycle number performed at this sweep rate), there is an accumulation of magnetite at the electrode surface. This consideration is supported by the results of Raman spectra that indicate the presence of magnetite in the whole potential range examined.

The two capacitances, C_1 and C_2, obtained from EIS measurements show maximum values at the potential range of peaks II and III (see Figs. 1 and 5). According to previous work [26], relatively high values, respectively, 1 and 100 mF cm^{-2}, correspond to the oxidation–reduction process on a highly subdivided surface texture. Magnetite is a good electronic conductor and the presence of Fe^0 small particles are in agreement with a large expanded surface area compared to a geometrical surface. When the electrode potentials become more anodic than the corresponding to peak VI, γ-Fe_2O_3 and/or γ-FeOOH, poor electronic conductors cover the electrode surface. C_1 becomes then smaller and approaches to the value of the interface (double layer) capacitance generally admitted.

In Fig. 6 it can be seen that beyond about −0.75 V, potential corresponding to peak IV, the emission of Fe^{2+} becomes smaller whereas that of Fe^{3+} increases up to this potential. This observation is in agreement with the formation of magnetite (Eqs. (4)–(6)), and a small part of species formed is dissolving. Moreover, in the reverse curve, at about −1 V, potential corresponding to peaks VII and VIII, the emission of Fe^{3+} starts decreasing due to the reduction of Fe^{3+} oxides (Eqs. (5) and (6)). This emission continues decreasing in peak IX (partial magnetite reduction) but at about −1.1 V (peaks X and XI) the formation of Fe_0 in the film (Eqs. (2) and (3)) seems to induce film electrical reorganisation with Fe^{3+} emission from the residual magnetite.

EQCM measurements allow evaluating the equivalent mass, M_e (g eq^{-1}) of oxides and/or hydroxides formed at the electrode surface by using Eq. (10).

$$M = \frac{\Delta m n F}{\Delta Q} \quad \text{and} \quad M_e = \frac{M}{n}, \tag{10}$$

where Δm and ΔQ represent, respectively, the changes in mass and charge involved between two data collections, n the number of charges involved in the oxidation–reduction process, M molar mass of the species involved, and F is Faraday constant.

Fig. 10 illustrates the results obtained according to Eq. (10). This curve is relative only to the third cycle, to avoid overcharging of the figure. Only one experimental point over 5 was kept here so that the mass change at each sampling point becomes less sensitive to scattering. Furthermore the mass loss due to the metal dissolution (cf. Fig. 6) is neglected, therefore, the equivalent mass calculated here is slightly underestimated. On this figure, some peak positions are also marked to easily compare the relationship to the voltammogram.

In the forward scan the equivalent mass is negative beyond peak V, corresponding to the expelling of electrolyte (water molecules). At peaks II and III, the film formation involves also a marked expelling of electrolyte giving to mass equivalent anomaly low (about −250 g eq^{-1}). A positive value observed at about −0.79 V corresponds, on the contrary, to the insertion of cations with water molecules, generally encountered, for instance, in the oxidation–reduction of electronic conducting polymers [27]. Though a significant mass change was observed in cathodic range ($E < -1.2$ V), major

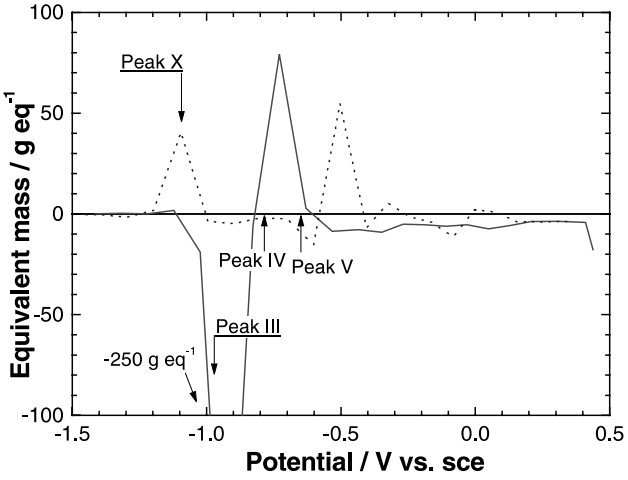

Fig. 10. Mass equivalent calculated from the results displayed in Fig. 7. Only the results relative to the anodic (–) and cathodic (- -) sweep at the third cycle are given here.

part of electrical charge is not involved in the formation of surface film, but mainly, as expected, in the hydrogen evolution reaction. This is the reason that makes the mass equivalent close to zero. The mass decrease corresponds also to the expelling of electrolyte or water molecules. The electrode potential rather than the oxidation state of surface film therefore mainly determines this process.

The surface film dehydration during the anodic scan and hydration during the cathodic scan for the potential range −0.7–0.4 V can also be deduced directly from the voltamassogram in Fig. 7. During the forward (anodic) scan mass decreases linearly with increasing potential, however, when the potential is scanned reversely, the slope is almost zero, i.e., the rate of mass loss (observable from cycle to cycle) is compensated by species (electrolyte) coming into the film structure.

The peak observed at about −0.5 V during the cathodic sweep is *not* significant since mass change and the charge involved in this range is small (Fig. 7). On the contrary, that observed near the peak X is significant and verifies by changing the number of sampling points. The mass equivalent calculated according to Eq. (2) is close to 40. That is, during the cathodic sweep, the reduction of Fe^{2+} into Fe^0 is accompanied by the mass gain of ca. 40 g eq^{-1}. This increase is due to the insertion of $[Na^+ \cdot H_2O]$ species, necessary to maintain the electrical neutrality. Such type of behaviour was observed on the nickel hydroxide layer [28,29]. When the electrode is polarised at a more cathodic potential range, neutral species such as electrolyte enters inside the surface oxide layer leading to the increase of the electrode mass. The hydrogen evolution reaction taking place at the electrode surface may enlarge the structure of surface film leading to the swelling. The origin of this process is unknown.

In situ Raman spectra show the magnetite presence in the whole interval of potentials (Fig. 2), between −1 and 0.5 V. The presence of α-FeOOH is evidenced at −0.53 V, (Raman signal at 398 cm^{-1}). At potentials more anodic, this species disappears (probably it dissolves, which will explain the small shoulder observed in Fig. 6 at about −0.6 V for Fe^{3+} emission in the anodic sweep) and oxides having the same crystallographic structure as magnetite start to appear. γ-Fe_2O_3 and/or γ-FeOOH are characterised by the peak at 710 cm^{-1}. The surface concentration of magnetite reaches a maximum at about −0.6 V for both potential sweeps.

The presence of magnetite in the whole potential range examined, and the oxidation processes taking place at the electrode surface can be explained if a double structure of the surface film is admitted. The inner film mainly composed by the magnetite, and the outer film of which composition depends upon the applied potential.

Beyond peak IV, where Fe^{3+} species are formed according to Eqs. (7) and (8), the ring-disk measurements (Fig. 6) show emission of Fe^{+3} only. Therefore, it can be considered that the external part of the passive layer is formed by species of Fe^{+3}. The emission rate of Fe^{+3} is not potential dependent. The chemical process for the formation of soluble Fe^{3+} species (for instance, FeOOH $+ H_2O \rightarrow Fe^{3+}_{aq.} + 3OH^-$) explains this phenomenon.

5. Conclusions

The results above presented and discussed allow formulating the following general conclusions:

1. In alkaline media free of aggressive anions, a passive layer based on magnetite protects iron. The results obtained in this work suggest that the surface film is composed of a three-dimensional structure in which the inner part remains Fe_3O_4 like in the whole potential range examined, and the outer part appears oxidised or reduced depending on the electrode potential.
2. Magnetite is formed at about −0.8 V thus, a spontaneous formation of magnetite on reinforcing steel bars embedded in concrete will take place at the open circuit potential even under low oxygen condition.
3. The redox processes developing in the passive film make very difficult to quantify rebar's corrosion rate in the cathodic potential domain (typically anaerobic conditions and/or cathodic protection imposed). Nevertheless, in the anodic domain (typically $E > -0.5$ V vs SCE) impedance measurements (through R_1 parameter) or linear polarisations performed at a suitable frequency (close to 1 mHz) will allow to estimate corrosion rate.

References

[1] Andrade C, Castelo V, Alonso C, González JA. The determination of the corrosion rate of steel embedded in concrete by the polarization resistance and ac impedance methods. In: Chaker V, editor. Corrosion Effect of Stray Currents and the Techniques for Evaluating Corrosion of Rebars in Concrete, ASTM STP 906. Philadelphia: American Society for Testing and Materials; 1986. p. 43–63.

[2] Gowers KR, Millard SG, Gill JS, Gill RP. Programmable linear polarisation meter for determination of corrosion rate of reinforcement in concrete structures. Br Corros J 1994;29(1):25–32.

[3] Stern M, Geary AL. Electrochemical polarization I. Theoretical analysis of the shape of polarization on curves. J Electrochem Soc 1957;104(1):56–63.

[4] Elsener B. Corrosion rate on reinforced concrete structures determined by electrochemical methods. Mater Sci Forum 1995;192–194:857–66.

[5] Glass GK, Page CL, Short NR, Zhang JZ. The analysis of potentiostatic transients applied to the corrosion of steel in concrete. Corros Sci 1997;39(9):1657–63.

[6] Videm K. Field and laboratory experience with electrochemical methods for assessing corrosion of steel in concrete. Mater Sci Forum 1998;289–292:3–14.
[7] Hachani L, Fiaud C, Triki E, Raharinaivo A. Characterisation of steel/concrete interface by electrochemical impedance spectroscopy. Br Corros J 1994;29(2):122–7.
[8] Hinatsu JT, Graydon WF, Foulkes RR. Voltammetric behaviour of iron in cement. III. Comparison of iron versus reinforcing steel. J Appl Electrochem 1991;21:425–9.
[9] Flis J, Pickering HW, Osseo-Asare K. Interpretation of impedance data for reinforcing steel in alkaline solution containing chlorides and acetates. Electrochim Acta 1998;43(12/13):1921–9.
[10] MacDonald DD, Roberts B. The cyclic voltammetry of carbon steel in concentrated sodium hydroxide solution. Electrochim Acta 1978;23:781–6.
[11] Zakroczymski T, Fan C-J, Szklarska-Smialowska Z. Kinetics and mechanism of passive film formation on iron in 0.05 M NaOH. J Electrochem Soc 1985;132(12):2862–7.
[12] Zakroczymski T, Fan C-J, Szklarska-Smialowska Z. Passive film formation on iron and film breakdown in a sodium hydroxide solution containing chloride ions. J Electrochem Soc 1985;132(12):2868–71.
[13] Juanto S, Zerbino JO, Míguez MI, Vilche JR, Arvia AJ. Ellipsometry of polycristalline iron electrodes in alkaline solutions containing chloride ions under different electrochemical conditions. Electrochim Acta 1987;32(12):1743–9.
[14] Haupt S, Streblow H-H. Layer formation and oxide reduction of passive iron in alkaline solution: a combined electrochemical and surface analytical study. Lagmuir 1987;3(6):873–85.
[15] Galindo MC, Martins ME, Vilche JR, Arvia A. Redox processes at iron hydroxide layers formed on platinum substrates in alkaline solutions. Electrochim Acta 1990;20:102–9.
[16] Hugot-Le Goff A, Flis J, Boucherit N, Joiret S, Wilinski J. Use of Raman spectroscopy and rotating split ring-disk electrode for identification of surface layers on iron in 1 M NaOH. J Electrochem Soc 1990;137(9):2684–90.
[17] Andrade C, Bolzoni F, Cabeza M, Nóvoa XR, Pérez MC. Measurement of steel corrosion in concrete by electrochemical techniques: influence of the redox processes in oxide scales. In: Electrochemical approach to selected corrosion and corrosion control studies, The European Federation of Corrosion series, Publication No 28. London: The Institute of Materials; 2000. p. 332–43.
[18] Taylor HFW. Cement Chemistry. 2nd ed. T. Telford Pub.; 1998. p. 214–15.
[19] Nóvoa XR, Pérez MC, Rangel C, Takenouti H. Anodic behaviour of iron in 1 M NaOH. In: 4th International Symposium on Electrochemical Impedance Spectroscopy. Rio de Janeiro, Brazil; August 1998. p. 300–03 [Extended abstracts].
[20] Andrade C, Alonso C, Keddam M, Nóvoa XR, Takenouti H. Impedance measurements on cement paste. Cem Conc Res 1997;27(8):1191–201.
[21] Andrade C, Keddam M, Nóvoa XR, Pérez MC, Rangel CM, Takenouti H. Electrochemical behaviour of steel rebars in concrete: influence of environmental factors and cement chemistry. In: 7th International Symposium on Electrochemical Methods in Corrosion Research, EMCR2000 Paper No. 045, 2000 May 28–June 1. Budapest, Hungary.
[22] Bouzek K, Rousar I. Influence of anode material on current yields during ferrate (VI) production by anodic iron dissolution. Part I: Current efficiency during anodic dissolution of grey cast iron to ferrate (VI) in concentrated alkali hydroxide solutions. J Appl Electrochem 1996;26:919–23.
[23] Larramona G, Gutiérrez C. The passive film of iron at pH 1–14. J Electrochem Soc 1989;136(8):2171–8.
[24] Beverskog B, Puigdomenech I. Revised Pourbaix diagrams for iron at 25–300°C. Corros Sci 1996;38(12):2121–35.
[25] Pérez MC. Corrosión de las armaduras en el hormigón: Estudio de los mecanismos de pérdida de la pasividad y modos de actuación para evitarla. PhD Thesis, University of Vigo, Spain, 1999.
[26] Andrade C, Merino P, Nóvoa XR, Pérez MC, Soler L. Passivation of reinforcing steel in concrete. Mater Sci Forum 1995;192–194:891–8.
[27] Izelt G, Bácskai J. Electrochemical quartz crystal microbalance study of the swelling of poly(vinylferrocene) films. Electrochim Acta 1992;37(4):647–54.
[28] P. Bernard. Étude par méthodes électrochimiques et électrogravimétriques de l'hidroxyde de nickel en couche mince au cours des processus de charge/décharge. Effects de quelques additifs. PhD Thesis, University Pierre et Marie Curie, Paris, France, 1992.
[29] Bernard P, Gabrielli C, Keddam M, Takenouti H, Leonardi J, Blanchard P. Ac quartz crystal microbalance applied to the studies of the nickel hydroxide behaviour in alkaline solutions. Electrochim Acta 1991;36(3/4):743–6.